Deposition of Three-Dimensional Graphene Aerogel on Nickel Foam as a Binder-Free Supercapacitor Electrode

Shibing Ye, Jiachun Feng,* and Peiyi Wu

State Key Laboratory of Molecular Engineering of Polymers, Department of Macromolecular Science and Laboratory of Advanced Materials, Fudan University, Shanghai 200433, China

S *Supporting Information*

ABSTRACT: We reported a new type of graphene aerogel–nickel foam (GA@NF) hybrid material prepared through a facile two-step approach and explored its energy storage application as a binder-free supercapacitor electrode. By simple freeze-drying and the subsequent thermal annealing of graphene oxide hydrogel–NF hybrid precursor, three-dimensional graphene aerogels with high mass, hierarchical porosity, and high conductivity were deposited on a NF framework. The resulting binder-free GA@NF electrode exhibited satisfactory double-layer capacitive behavior with high rate capability, good electrochemical cyclic stability, and a high specific capacitance of 366 F g^{-1} at a current density of 2 A g^{-1}. The versatility of this approach was further verified by the successful preparation of 3D graphene/carbon nanotube hybrid aerogel–NF as a supercapacitor electrode, also with improved electrochemical performance. With advantageous features, such a facile and versatile fabrication technique shows great promise in the preparation of various types of carbon–metal hybrid electrodes.

KEYWORDS: *graphene, nickel foam, aerogel, supercapacitor, electrode*
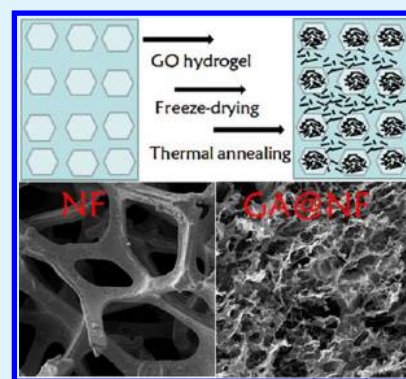
1. INTRODUCTION

Supercapacitors as one of the most important types of devices for next-generation energy storage have attracted increasing attention due to their desirable features including high power density, fast charging–discharging rate, and excellent cycle stability.[1-3] On the basis of the mechanism of energy storage, supercapacitors can be categorized into two classes: electrochemical double-layer capacitors (EDLCs) and pseudocapacitors. EDLCs store energy through reversible adsorption of anions and cations at the electrode–electrolyte interface, the capacitance of which is generally dependent on the specific surface area of the electrode materials. In contrast, pseudocapacitors store energy through fast surface redox reactions of the electrode material with the electrolyte.[4] Currently, the electrodes used in most commercial supercapacitors are made of inexpensive and corrosion-resistant carbon materials.[5] The carbon-based supercapacitors are EDLCs, which typically have better cyclic stability and longer service lifetime than pseudocapacitors.[6] Over the past years, carbon materials such as activated carbon, mesoporous carbon, and carbon nanotubes (CNTs) have been extensively investigated as the electrodes for EDLCs.[7-10] The mature fabrication strategies and improved understanding of the storage mechanism of EDLCs have paved the way for the development of supercapacitors based on new electrode materials.

Recently, graphene, an atom-thick two-dimensional (2D) carbon nanostructure, has become an attractive candidate as a building block for electrodes of EDLCs.[11-17] Compared with traditional porous carbon materials, graphene has a very high electrical conductivity, large surface area, and profuse interlayer structure, theoretically meeting the requirements of high-performance supercapacitors.[18-20] Various graphene-based materials, including chemical vapor deposition graphene, chemically reduced graphene oxide (GO), and thermally reduced GO, have been extensively studied as electrodes for supercapacitors and exhibited good electrochemical performance.[21-25] Despite their advantages, graphene-based electrodes face two important technical limitations: self-aggregation of graphene sheets and contact resistance between graphene and the metal current collector.[26] The first one, the aggregation tendency of graphene, dramatically decreases the specific surface area of graphene-based electrodes, which hinders the ion diffusion from the electrolyte to the electrodes and reduces the effective capacitance.[27] To solve this problem, graphene sheets are generally assembled into a three-dimensional (3D) architecture that would effectively prevent the restacking of graphene sheets and maintain their high specific surface area, thus resulting in good capacitive performance.[28] Using strategies such as the hydrothermal method,[12,29] template method,[14,30] and chemical reduction,[31,32] various 3D graphene-based materials including aerogels, foams, and sponges have been successfully prepared and applied as supercapacitors. As for the second limitation, how to attach the 3D graphene-based materials onto the metal current collector with low contact resistance is another substantial challenge. In a lot of cases, although the graphene-based materials possess high electrical conductivity and large

surface area, the graphene-based supercapacitors still have not met the expected performance, mainly due to the higher contact resistance. In this regard, several intelligent strategies such as electrophoretic deposition,[33] chemical vapor deposition,[34] and vacuum filtration deposition[35] have been developed to prepare binder-free electrodes, where the active materials directly "grow" on the metal substrate. By using these ways, one can improve the internal binding between active materials and metal current collectors and thus produce electrodes with very small resistances. However, note that the approaches for fabricating graphene-based electrodes that can simultaneously overcome the aforementioned two technical limitations have barely been reported. Until just recently, Shi et al.[36] pioneered the method of depositing 3D graphene hydrogel in the micropores of nickel foam (NF) to form a composite electrode for high-rate electrochemical capacitors. In their work, the graphene hydrogel−NF composite electrode was obtained by immersing and heating the NF filled with GO suspension in the solution of reducing agent.

In previous studies, GO aerogels were found to be readily produced by simple freeze-drying of GO concentrated dispersions.[37,38] Recent achievements have demonstrated that thermal reduction of GO aerogel is a promising method for preparing graphene aerogel, which could effectively prevent graphene sheets from self-stacking that always occurs during chemical reduction and the hydrothermal process.[39] Inspired by these findings, here we propose a more facile and scalable approach to prepare 3D graphene aerogel−NF hybrid material as the binder-free electrode for EDLCs. By simple freeze-drying and the subsequent thermal annealing of the graphene oxide hydrogel−NF hybrid precursor, 3D and high-mass graphene aerogel with hierarchical porosity and high conductivity was deposited on a NF framework. The resulting binder-free GA@NF electrode exhibited satisfactory double-layer capacitive behavior with high rate capability, good electrochemical cyclic stability, and a high specific capacitance of 366 F g^{-1} at a current density of 2 A g^{-1}. Efforts have also been made to achieve synergistic integration of 2D graphene sheets and one-dimensional CNTs, where the electrode based on the graphene/CNT aerogel−NF hybrid electrode was successfully prepared through a similar method, demonstrating the versatility of this novel deposition method for preparing 3D carbon−metal hybrid materials.

2. EXPERIMENTAL SECTION

2.1. Preparation of GA@NF and GCA@NF. GO was prepared by oxidation of natural graphite (Qingdao BCSM Co., Ltd., China) according to a modified Hummers method.[40] The NF sheets (Changsha Lyrun New Material Co. Ltd., China) with a size of 2 cm × 1 cm × 0.1 cm were thermally treated at 1000 °C in Ar before use. All the other reagents were supplied from Aldrich and Sinopharm Chemical Reagent Co. Ltd. and used as received. As shown in Figure 1, the preparation of graphene aerogel deposited onto NF (labeled as GA@NF) mainly consists of two steps: the precursor GO aerogel is formed in situ on the
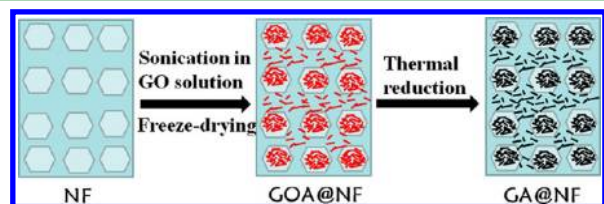

Figure 1. Scheme for the fabrication of the GA@NF.

NF framework, followed by thermal reduction under an Ar atmosphere. Typically, the graphite oxide was dispersed in deionized water by ultrasonication to acquire GO aqueous dispersions (6 mg mL^{-1}). Then, a weighed NF sheet was immersed into the above GO dispersions, followed by ultrasonication for another 1 h and aging for 24 h at 60 °C. Afterward, the NF sheet filled with wet GO gel was suddenly frozen with liquid nitrogen and freeze-dried for 3 days under a vacuum to form GO aerogel deposited on NF, which was labeled as GOA@NF. In the second step, GOA@NF was annealed at 400 °C for 1 h in a tube furnace (Shanghai GuangShu Electrical Co., Ltd., China) under a flowing stream of Ar. Before heating, the tube was purged with Ar for 30 min, and the heating rate was set at 15 °C min^{-1}. The resulting GA@NF was collected after the furnace was cooled slowly back to room temperature under flowing Ar. According to the statistical results listed in Table S1 (Supporting Information), the surface mass density of GA in GA@NF is ∼1.0 mg cm^{-2}.

To verify the versatility of the above method, we also employed the mixture of GO and CNT (Chengdu Organic Chemical Co., Ltd., China) as the starting material for carbon−metal hybrid electrodes. Predispersed GO sheets and CNTs were mixed and sonicated by adding 1 wt % sodium dodecyl sulfate to obtain homogeneous GO/CNT (50/50, wt) complexes (6 mg mL^{-1}). The graphene/CNT aerogel−NF (labeled as GCA@NF) was prepared in a similar procedure as that of GA@NF. Briefly, the wet gel of the GO/CNT complexes deposited on NF substrate was obtained through ultrasonication and aging, and then underwent freeze-drying and thermal annealing to produce GCA@NF. It should be pointed that our graphene was prepared by thermally reducing GO at 400 °C; thus, the so-called graphene is essentially the reduced GO (rGO).

2.2. Characterizations. GO and rGO aerogel were scraped from the surfaces of NF and used for structural and chemical characterizations. Scanning electron microscopy (SEM, TESCAN 5136 MM) was applied to observe the surface morphologies of NF, GOA@NF, GA@NF, and GCA@NF at an operating voltage of 20 kV. X-ray diffraction (XRD, PANalytical X'pert PRO) was carried out with Cu Kα radiation at an accelerating voltage of 40 kV and a current of 25 mA. X-ray photoelectron spectroscopy (XPS, Kratos AXIS Ultra^{DLD}) was used to determine the chemical composition of GO and rGO aerogels. The specific surface area based on GA that separated from GA@NF was obtained using a Brunauer−Emmett−Teller apparatus (BET, Micromeritics, ASAP2020). The electrical conductivity of rGO treated under the same condition as the preparation of GA@NF was measured by a four-probe method at room temperature. GO and GO/CNT hybrid were observed with a transmission electron microscope (TEM, JEOL JEM2100F).

2.3. Electrochemical Measurements. All electrochemical measurements were carried out in a conventional three-electrode system using an electrochemical workstation (CHI660D, Chenhua Instruments, China) with 6 M KOH solution as the electrolyte. The as-prepared porous materials including GA@NF and GCA@NF were directly tested as the electrode, while saturated calomel electrode (SCE) as the reference and a platinum plate as the counter electrode. The electrochemical performances of the prepared electrodes were characterized by cyclic voltammetry, electrochemical impedance spectroscopy measurements, and galvanostatic charge−discharge tests. The specific capacitance was obtained from the discharge process according to the following equation, Cs (F/g) = $I\Delta t/\Delta Em$, where I is the current loaded (A), Δt is the discharge time (s), ΔE is the potential change during the discharge process, and m is the mass of active material (g).[41] In our electrochemical tests, the mass of active materials within both GA@NF and GCA@NF electrodes was approximately 0.8 mg.

3. RESULTS AND DISCUSSION

3.1. Morphology and Chemical Structure of GA@NF. Our previous study found that GO aerogel could be obtained by directly freeze-drying the GO concentrated aqueous dispersions, but these GO aerogels without gelation showed extreme fragility.[37] Nguyen et al.[42] found that simple ultrasonication could induce the gelation of GO aqueous dispersions, which
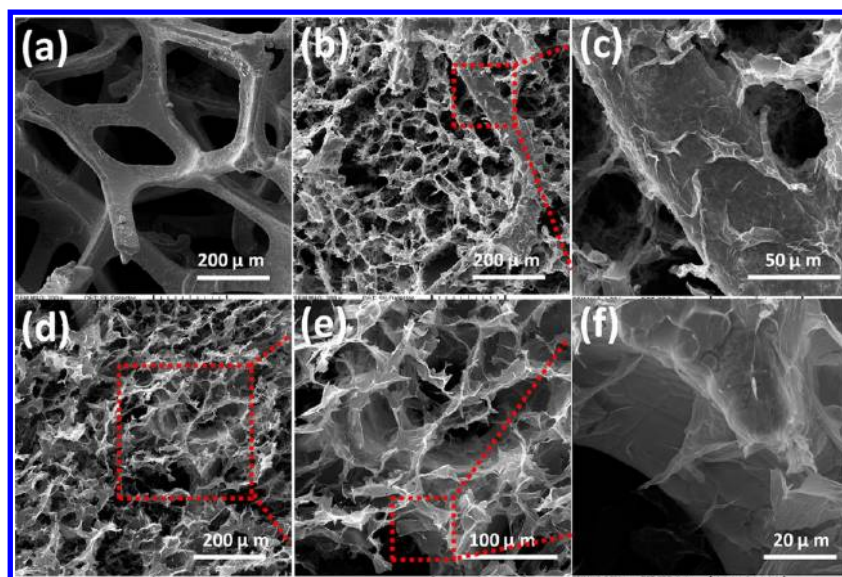
Figure 2. SEM images of (a) NF, (b, c) as-prepared GOA@NF at different magnifications, and (d−f) as-prepared GA@NF at different magnifications.
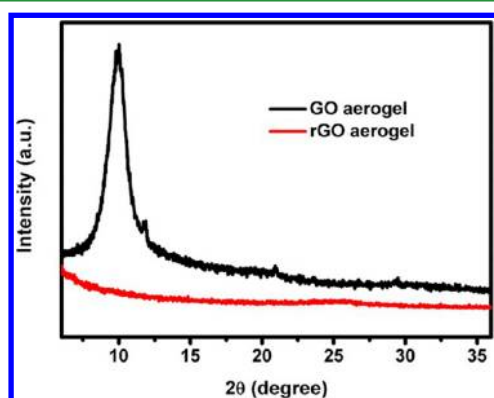

Figure 3. XRD patterns of GO aerogel and rGO aerogel.

allows for the in situ formation of the relatively strong GO aerogel. As shown in Figure S1a (Supporting Information), the free-flowing GO aqueous dispersions cannot form hydrogel before any treatments. On the contrary, with the aid of simple ultrasonication of the precursor aqueous dispersions, GO hydrogel containing a NF sheet is easily generated (Figure S1b, Supporting Information), which should be due to the decrease in the lateral dimensions of the nanosheets.[42] This sonication-induced gelation leads to fully filling of a mass of GO into NF micropores (Figure S1c, Supporting Information), suggesting strong adhesion of GO onto NF and favorable interactions between GO sheets. The optical images also show that GO aerogel changes color from yellow for GOA@NF to black for GA@NF, obviously indicating the reduction of GO during thermal annealing. It was observed in GA@NF that an abundance of graphene was deposited onto NF substrate, which is necessary to store enough electricity, overcoming the limitation of other fabrication methods that could only deposit a limited amount of graphene on NF.[33−35]

SEM images of NF, GOA@NF, and GA@NF are shown in Figure 2. Compared with the bare NF with a 3D cross-linked grid structure (Figure 2a), GOA@NF displays an entirely different morphology, where 3D GO networks fill into the interspace and coat on the frameworks of NF. GO nanosheets assemble into an amorphous and interconnected porous structure with pore sizes

in the range of several micrometers to dozens of micrometers (Figure 2b), which is driven by various interactions including van der Waals attractions, hydrogen bonding between functional groups, and $\pi-\pi$ stacking of residual sp^2-hybridized regions on the basal plane.[42] High-magnification observation of GOA@NF reveals that crumpled and scrolled GO sheets are tightly covered on the surface of NF (Figure 2c), suggesting good contact between GO sheets and metal substrate. Figure 2d−f shows the morphology of the rGO aerogel deposited on NF in the GA@NF. Interestingly, there is no obvious difference in the morphology of the aerogel before (Figure 2b) and after thermal annealing at 400 °C (Figure 2d), which indicates that rGO aerogel maintains the original 3D structure of GO aerogel. The strength of GO aerogel itself along with the modest heating rate may be the most likely reason for the preservation of 3D structure.[43] Moreover, from the high magnification images (Figure 2e and f), the rGO sheets without apparent aggregation are also observed to be attached to the NF substrate. XRD patterns in Figure 3 demonstrate that the typical diffraction peak of GO at 10° disappears in the pattern of rGO aerogel owing to the removal of the oxygen-containing groups from GO layers. However, no obvious graphite diffraction peaks are observed for the rGO aerogel, further confirming that rGO aerogel deposited on NF has an amorphous structure, without significant restacking of graphene sheets after thermal reduction.[28,44]

To further investigate the changes of oxygen-containing species during the reduction process, XPS analyses are conducted for both the GO and rGO aerogels. Figure 4 shows the C 1s spectra, which can be curve-fitted into four peak components with BEs at about 284.4, 286.5, 287.5, and 288.9 eV, attributable to the C—C, C—O, C=O, and O—C=O species, respectively. Comparing the two spectra in Figure 4a and b, the marked decrease in the intensities of peaks associated with oxygenated groups suggests that partial oxygen-containing functional groups of GO were removed by thermal reduction at 400 °C. The wide scan XPS spectra in Figure 4c show that the C/O atomic ratios are 2.2 and 6.5 for GO and rGO aerogels, respectively. Note that the C/O atomic ratio of rGO further increased to 18.1 when the annealing temperature was increased to 800 °C (Figure S3, Supporting Information). Moreover, this value was reported to be as high as 65 at the treating temperature
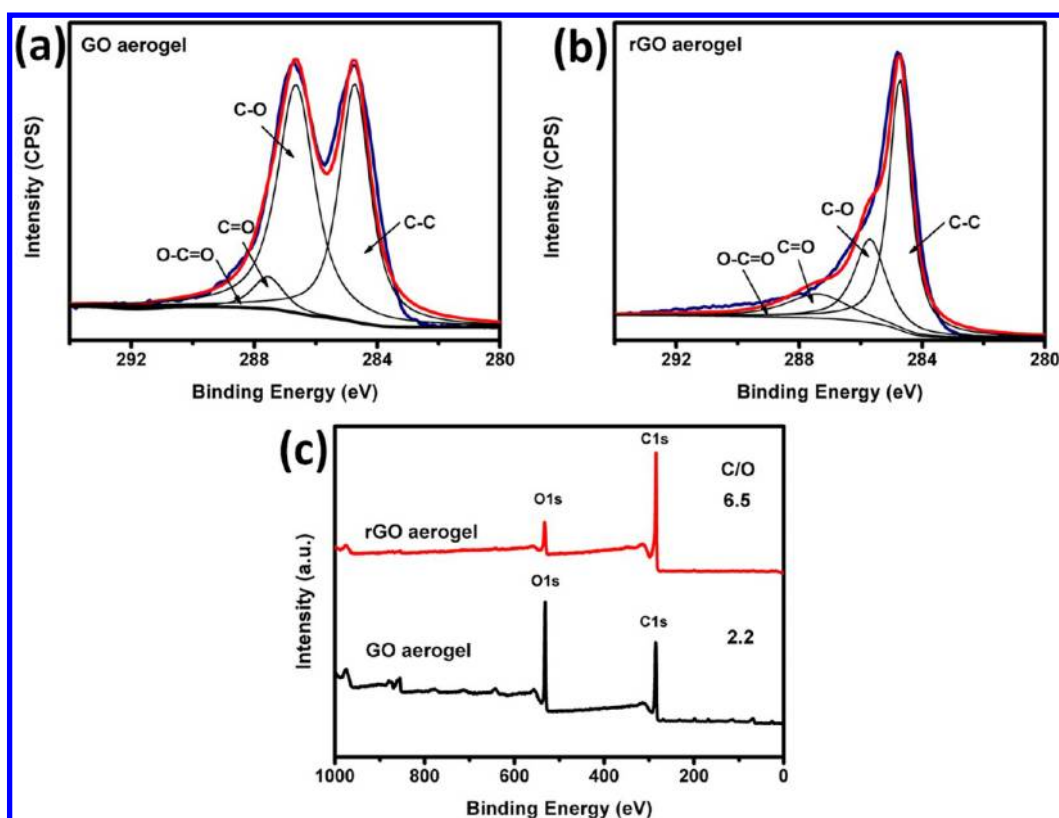
7124

dx.doi.org/10.1021/am401458x | *ACS Appl. Mater. Interfaces* 2013, 5, 7122−7129

Figure 4. The C 1s XPS spectra for (a) GO aerogel and (b) rGO aerogel as well as (c) the wide scan XPS spectra of GO and rGO aerogel.
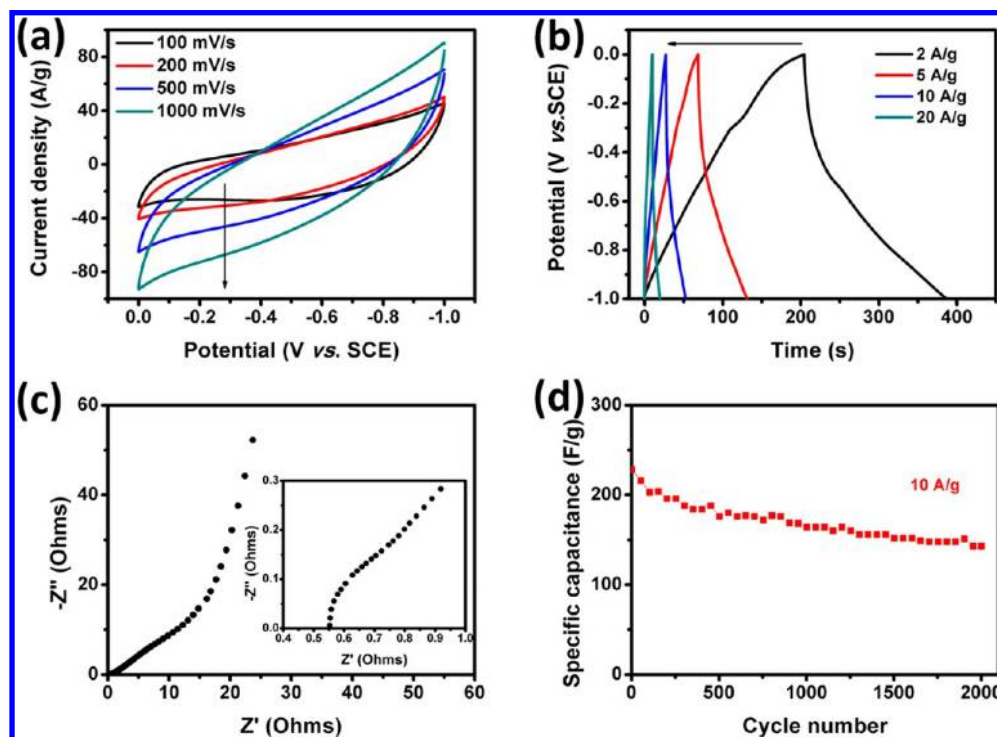

Figure 5. Electrochemical performance of the GA@NF electrode in 6 M KOH solution: (a) CV curves at various scan rates; (b) GCD curves under different current densities; (c) Nyquist plot for GA@NF (the inset shows the high-frequency region of the plot); (d) cycle stability tests at a current density of 10 A g^{-1}.

of 1100 °C.[45] All of this is just to say that there remain partially oxygen-containing functional groups on rGO sheets that are treated at 400 °C.

In this study, the combination of freeze-drying and thermal reduction not only generates 3D graphene aerogel deposited on NF but also prevents the restacking of graphene sheets during the reduction process of GO, which will increase the specific surface
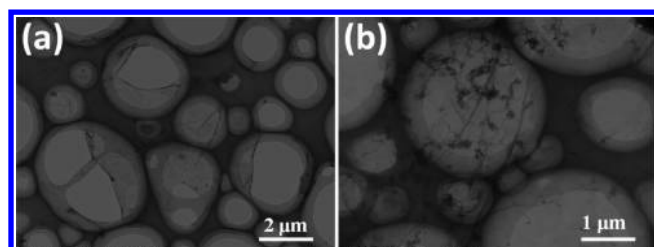
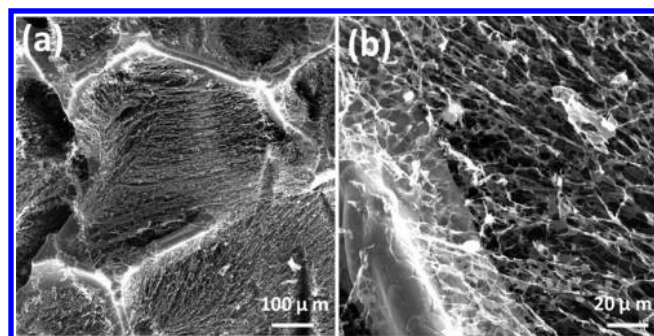**Figure 6.** TEM images of (a) GO sheets and (b) GO/CNT hybrid.

Figure 7. SEM images of as-prepared GCA@NF at different magnifications (a, b).

area of GA@NF. The BET nitrogen adsorption isotherm (Figure S2, Supporting Information) reveals a large specific surface area for rGO aerogel of 463 m^2 g^{-1}, suggesting the predominant macroporous structure in consistence with SEM observation (Figure 2d−f). Meanwhile, the rGO obtained from the thermal treatment of GO at 400 °C shows an electrical conductivity as high as 71.4 S m^{-1}, which should be attributed to the partial removal of oxygen-containing groups and the restoration of a

conjugated network of graphene. The large specific surface area, together with the high conductivity of rGO, makes GA@NF a favorable electrode material for many applications.[4,21]

3.2. Electrochemical Performance of GA@NF. The use of graphene−NF hybrid materials as EDLCs has also been reported previously.[33−36] Because of its large specific surface area, high conductivity, high-quality contact interface, and sufficient quantity of active material, GA@NF is expected to be an excellent choice for electrode materials of supercapacitors. Figure 5a shows the cyclic voltammograms (CVs) of GA@NF at different scan rates from 100 to 1000 mV s^{-1}. At a scan rate of 100 mV s^{-1}, the CV curve exhibits typical quasi-rectangular shape, characteristic of the double-layer capacitor, indicating good charge propagations at the electrode interfaces following the EDLC mechanism.[46] With an increase in scan rate, the current response increases accordingly, and the CV curves keep their quasi-rectangular shape with small distortions, which implies that the GA@NF electrode has good rate performance and low internal resistance for the graphene−NF interface. However, obvious redox peaks could be observed in the CV curve at a lower scan rate of 20 mV s^{-1} (Figure S4a, Supporting Information), indicating the existence of pseudocapacitance, which should be attributed to the remaining oxygen-containing groups of rGO.

As shown in Figure 5b, the galvanostatic charge−discharge (GCD) curves at four different current densities exhibit nonsymmetric triangular shape, which is also the signal of the existence of pseudocapacitance besides electric double layer capacitance. The specific capacitance calculated from the GCD curve is 366 F g^{-1} at a current density of 2 A g^{-1}, which is comparable to the best performance of supercapacitors made with graphene or GO in recent reports.[12,47] Such a high specific capacitance of GA@NF should be attributed to the residual oxygen functional groups of rGO and the high specific surface
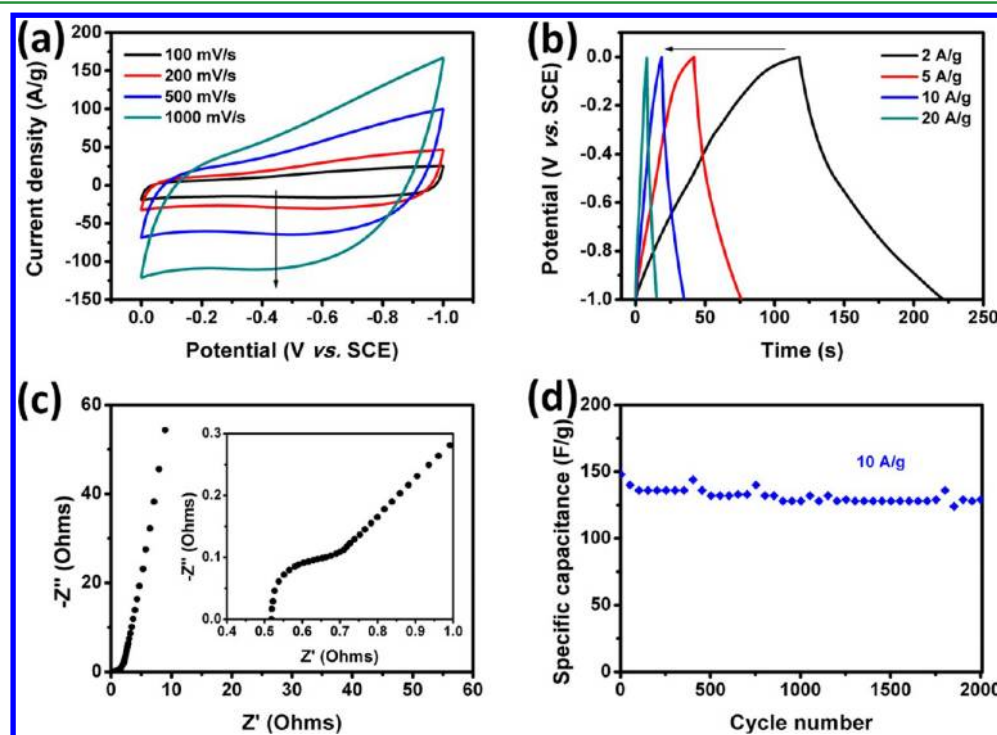

Figure 8. Electrochemical performance of the GCA@NF electrode in 6 M KOH solution: (a) CV curves at various scan rates; (b) GCD curves under different current densities; (c) Nyquist plot for GCA@NF (the inset shows the high-frequency region of the plot); (d) cycle stability tests at a current density of 10 A g^{-1}.

area of rGO aerogel. On the one hand, the abundant oxygen functional groups not only introduce large peseudocapacitance but also enhance the wettability of the electrode and improve electrolyte ionic accessibility.[15,48,49] On the other hand, 400 °C is reported to be the optimal treating temperature for preparing graphene with the highest BET surface area, which helps the resulting materials obtain a higher specific capacitance.[16,17,23] The GCD curves also display that the GA@NF electrode maintains its 49% specific capacitances with a value of 186 F g^{-1} as the current density is increased 10-fold from 2 to 20 A g^{-1}, indicating high-rate performance. This is probably due to the high conductivity of rGO aerogels which accelerates the charge transfer during the discharge processes at high current densities.[25]

To better understand the rate performance of the GA@NF electrode, the kinetic feature of the ion diffusion in this electrode is investigated using electrochemical impedance spectroscopy (EIS). Figure 5c shows the Nyquist plot based on a frequency response analysis of frequencies ranging from 1 MHz to 10 mHz. The impedance curve intersects the real axis at a 45° angle in the beginning, which is the typical feature of a porous electrode when saturated with electrolyte.[50] At low frequencies, the straight line tends to be perpendicular to the real axis, indicating the pure capacitive behavior of GA@NF.[13,36] The inset in Figure 5c shows the magnified data in the high-frequency range. The equivalent series resistance (ESR) of GA@NF obtained from the x-intercept of the Nyquist plot is extremely small at ~0.45 Ω, and this relatively small ESR is due to the existence of a 3D network structure that can facilitate the efficient access of electrolyte ions to the graphene surface and shorten the ion diffusion path.[51]

The cycle stability of the assembled supercapacitor was evaluated by repeating the GCD test between 0 and −1.0 V at a current density of 10 A g^{-1}. As shown in Figure 5d, the capacitance retention of the GA@NF electrode reaches ~60% after 2000 cycles. Theoretically, both the 3D network structure allowing for easy access of ions and the improved electrical conductivity suggest a potentially good cycling stability for the GA@NF electrode. However, the relatively large capacitance degradation (~40%) may be mainly attributed to the presence of residual oxygen functional groups on rGO. These redox sites are insufficiently stable for repeated insertion/deinsertion of counterions, and will be neutralized and diminished by alkaline KOH during repeating charging−discharging cycles, causing the loss of pseudocapacitance.[48] A comparative experiment (Figure S4, Supporting Information) based on GA@NF treated at a higher temperature of 800 °C confirmed this conclusion. Compared with the electrode treated at 400 °C, the GA@NF electrode with a higher C/O atomic ratio (18.1) of rGO exhibits better cycle stability with ~85% capacitance retention and a smaller specific capacitance (116 F g^{-1} at a current density of 2 A g^{-1}). The remaining functional groups contribute to the high capacitance, but they simultaneously impair cycle life. Therefore, it is significant for us to find a suitable annealing temperature to balance the specific capacitance and cycle stability. Still, it is undeniable that GA@NF used as a electrode for a supercapacitor presents excellent electrochemical performance and that this novel fabrication approach may open up an opportunity for preparing other types of carbon−metal hybrid electrodes.

3.3. Preparation, Morphology, and Electrochemical Performance of GCA@NF.

Compared with the existing methods for preparing carbon−metal hybrid electrodes, the approach proposed in this work is not only easy to operate and reproduce on a large scale but can also be used to prepare a variety of other types of carbon−metal hybrid materials. If various additives, i.e., CNTs and doped elements, can be further introduced into graphene aerogels during deposition, the potential applications of the resulting materials will also expand to fuel cells and supercapacitors. To demonstrate this versatility, we fabricated a hybrid electrode (GCA@NF) where graphene/CNT hybrid aerogels are deposited onto NF using the similar technique as the preparation of GA@NF.

Graphene sheets and CNTs are usually assembled into hybrid aerogel to integrate the intriguing properties of graphene sheets and CNTs, creating new bulk materials with desired structures and charming properties.[8,26,52] Given that CNTs can bridge the defects for electron transfer as well as increase the layer spacing between graphene sheets, the combination of graphene sheets and CNTs holds great promise in the application of supercapacitor.[30,47,53] Since GO is an amphiphile with hydrophilic edges and a more hydrophobic basal plane, it can act as a colloidal surfactant to assist the dispersion of hydrophobic CNTs in aqueous solution.[54,55] TEM images in Figure 6 reveal that the CNTs are well linked and distributed uniformly on the surface of GO sheets, indicating that GO sheets are able to disperse CNTs in aqueous solution. There are no CNT bundles or large agglomerated particles other than small particles observed on the GO surface, which guarantees that CNTs are uniformly dispersed in GO in the hybrid wet gel. Likewise, the corresponding rGO/CNT aerogel is obtained by freeze-drying the wet gel, followed with thermal reduction at 400 °C. It is worth noting that the binder-free rGO−CNT aerogel maintains intact and unchallenged after the reduction of GO, which should be ascribed to the strong interaction between rGO sheets and CNTs.

Figure 7 shows the microstructure of rGO/CNT aerogels in GCA@NF at different magnifications, which is obviously different from the rGO aerogel in GA@NF. As shown in Figure 7a, the low-magnification view illustrates its general morphology in which rGO and CNT assemble into well-defined fibrous nanostructures, also constituting a continuous 3D network structure. Furthermore, there is no apparent sign of stacked rGO sheets or aggregated CNTs, suggesting a uniform distribution of CNTs in the matrix of rGO that can effectively prevent the restacking of rGO sheets. Either CNTs or rGO sheets are dispersed uniformly in the aerogel matrix because CNTs can be well dispersed and stabilized in GO dispersions before reduction (Figure 6b). This is further confirmed by the high-magnification view of the morphology (Figure 7b), which provides a clearer picture of the morphology of GCA@NF. The rGO−CNT hybrid aerogel exhibits a unique 3D network composed of randomly oriented CNTs, wrinkled rGO sheets, and a lot of irregular pores. Generally, this hierarchically porous structure may favor mass transfer and reduce transport limitation for the hybrid aerogels in some particular applications such as supercapacitors.

The electrochemical performance of the GCA@NF-based electrode was also investigated using the same methods including CV, GCD, and EIS tests. As expected, the GCA@NF electrode in the three-electrode system presents a high-performance capacitive behavior. Figure 8a shows the CV curves of the GCA@NF electrode with different scan rates, which exhibit an approximately rectangular shape. No obvious distortion in the curves is observed even at a scan rate of 1000 mV s^{-1}, indicative of perfect EDLC behavior and a fast charging−discharging process.[41] Accordingly, the GCD curves at different current densities in Figure 8b exhibit a symmetric triangle feature with little potential drop. GCA@NF presents a specific capacitance of

207 F g^{-1} at a current density of 2 A g^{-1}, lower than that of GA@NF, which could be due to the effect of additional CNT with lower capacitance compared to rGO sheets.[26] As the current density increases to 20 A g^{-1}, the specific capacitance of the GCA@NF electrode remains at 142 F g^{-1}, also exhibiting a good rate performance. As shown in Figure 8c, the Nyquist plot of the GCA@NF electrode exhibits a small semicircle over the high frequency range, and the ESR calculated from the x-intercept on the plot is ~0.51 Ω. Moreover, GCA@NF has a quite straight line in the low frequency region, probably due to the lower diffusion resistance by the shortened proton diffusion path in rGO−CNT aerogel.[25,56] The repeated GCD tests reveal that GCA@NF exhibits better cycling stability than GA@NF. After 2000 cycles, the specific capacitance still remains at about 80% of initial performance, much higher than 60% for GA@NF (Figure 8d). This improvement could be attributed to the addition of CNTs, which usually shows better cycling stability due to the nonexistence of the pseudocapacitance effect.[8,26] The above results show that GCA@NF has unique advantages as a new type of electrode material for high performance supercapacitors.

4. CONCLUSIONS

In this work, three-dimensional graphene aerogel was successfully anchored on a porous nickel framework by freeze-drying and thermal annealing the graphene oxide hydrogel−nickel foam precursor. The resulting graphene aerogel−nickel foam hybrid material was used as a binder-free electrode for supercapacitors, which exhibited excellent double-layer capacitive behavior including high rate capability, good electrochemical cyclic stability, and a high specific capacitance of 366 F g^{-1} at a current density of 2 A g^{-1}. The good electrochemical performance originates from the synergistic effect of the hierarchically porous structure, large specific surface area, high conductivity, low contact resistance, and sufficient deposition mass of graphene aerogel. By using a similar method, a graphene/CNT aerogel−nickel foam hybrid electrode was prepared, which also presented good electrochemical performance with better cycling stability than the graphene aerogel−nickel foam hybrid electrode. Therefore, this is a novel, facile, and versatile approach that shows great promise in the preparation of various types of carbon−metal hybrid electrodes.

■ ASSOCIATED CONTENT

Ⓢ Supporting Information

Photographs of GO hydrogel, NF, GOA@NF, and GA@NF; BET isotherm graph of rGO aerogel; XPS of rGO treated at 800 °C; electrochemical performance of GA@NF treated at 800 °C; electrochemical performance of GA@NF measured in the two-electrode system; TGA of sodium dodecyl sulfate; and complete results of the weight of NF and GA@NF samples. This material is available free of charge via the Internet at http://pubs.acs.org.

■ AUTHOR INFORMATION

Corresponding Author

*E-mail: jcfeng@fudan.edu.cn. Phone: 86 (21) 6564 3735. Fax: +86- 21-6564 0293.

Notes

The authors declare no competing financial interest.

■ ACKNOWLEDGMENTS

■ REFERENCES

(1) Zhang, L. L.; Zhao, X. S. *Chem. Soc. Rev.* **2009**, *38*, 2520−2531.

(2) Snook, G. A.; Kao, P.; Best, A. S. *J. Power Sources* **2011**, *196*, 1−12.

(3) Zhi, M. J.; Xiang, C. C.; Li, J. T.; Li, M.; Wu, N. Q. *Nanoscale* **2013**, *5*, 72−88.

(4) Huang, Y.; Liang, J. J.; Chen, Y. S. *Small* **2012**, *8*, 1805−1834.

(5) Jiang, H.; Lee, P. S.; Li, C. Z. *Energy Environ. Sci.* **2013**, *6*, 41−53.

(6) Ghosh, A.; Lee, Y. H. *ChemSusChem* **2012**, *5*, 480−499.

(7) Zhai, Y. P.; Dou, Y. Q.; Zhao, D. Y.; Fulvio, P. F.; Mayes, R. T.; Dai, S. *Adv. Mater.* **2011**, *23*, 4828−4850.

(8) Nardecchia, S.; Carriazo, D.; Ferrer, M. L.; Gutierrez, M. C.; del Monte, F. *Chem. Soc. Rev.* **2013**, *42*, 794−830.

(9) Hahm, M. G.; Reddy, A. L. M.; Cole, D. P.; Rivera, M.; Vento, J. A.; Nam, J.; Jung, H. Y.; Kim, Y. L.; Narayanan, N. T.; Hashim, D. P.; Galande, C.; Jung, Y. J.; Bundy, M.; Karna, S.; Ajayan, P. M.; Vajtai, R. *Nano Lett.* **2012**, *12*, 5616−5621.

(10) Noked, M.; Soffer, A.; Aurbach, D. *J. Solid State Electron.* **2011**, *15*, 1563−1578.

(11) El-Kady, M. F.; Strong, V.; Dubin, S.; Kaner, R. B. *Science* **2012**, *335*, 1326−1330.

(12) Zhao, Y.; Hu, C. G.; Hu, Y.; Cheng, H. H.; Shi, G. Q.; Qu, L. T. *Angew. Chem., Int. Ed.* **2012**, *51*, 11371−11375.

(13) Zhang, L. L.; Zhao, X.; Stoller, M. D.; Zhu, Y. W.; Ji, H. X.; Murali, S.; Wu, Y. P.; Perales, S.; Clevenger, B.; Ruoff, R. S. *Nano Lett.* **2012**, *12*, 1806−1812.

(14) Lee, S. H.; Kim, H. W.; Hwang, J. O.; Lee, W. J.; Kwon, J.; Bielawski, C. W.; Ruoff, R. S.; Kim, S. O. *Angew. Chem., Int. Ed.* **2010**, *49*, 10084−10088.

(15) Biswas, S.; Drzal, L. T. *ACS Appl. Mater. Interfaces* **2010**, *2*, 2293−2300.

(16) Zhang, L.; Zhang, F.; Yang, X.; Long, G. K.; Wu, Y. P.; Zhang, T. F.; Leng, K.; Huang, Y.; Ma, Y. F.; Yu, A.; Chen, Y. S. *Sci. Rep.* **2013**, *3*, 1408.

(17) Zhang, L.; Yang, X.; Zhang, F.; Long, G. K.; Zhang, T. F.; Leng, K.; Zhang, Y. W.; Huang, Y.; Ma, Y. F.; Zhang, M. T.; Chen, Y. S. *J. Am. Chem. Soc.* **2013**, *135*, 5921−5929.

(18) Huang, X.; Zeng, Z. Y.; Fan, Z. X.; Liu, J. Q.; Zhang, H. *Adv. Mater.* **2012**, *24*, 5979−6004.

(19) Kuila, T.; Mishra, A. K.; Khanra, P.; Kim, N. H.; Lee, J. H. *Nanoscale* **2013**, *5*, 52−71.

(20) Mao, S.; Wen, Z. H.; Kim, H.; Lu, G. H.; Hurley, P.; Chen, J. H. *ACS Nano* **2012**, *6*, 7505−7513.

(21) Cao, X. H.; Shi, Y. M.; Shi, W. H.; Lu, G.; Huang, X.; Yan, Q. Y.; Zhang, Q. C.; Zhang, H. *Small* **2011**, *7*, 3163−3168.

(22) Zhu, Y. W.; Murali, S.; Stoller, M. D.; Ganesh, K. J.; Cai, W. W.; Ferreira, P. J.; Pirkle, A.; Wallace, R. M.; Cychosz, K. A.; Thommes, M.; Su, D.; Stach, E. A.; Ruoff, R. S. *Science* **2011**, *332*, 1537−1541.

(23) Zhang, H. X.; Bhat, V. V.; Gallego, N. C.; Contescu, C. I. *ACS Appl. Mater. Interfaces* **2012**, *4*, 3239−3246.

(24) Zhao, B.; Liu, P.; Jiang, Y.; Pan, D. Y.; Tao, H. H.; Song, J. S.; Fang, T.; Xu, W. W. *J. Power Sources* **2012**, *198*, 423−427.

(25) Zhang, L.; Shi, G. Q. *J. Phys. Chem. C* **2011**, *115*, 17206−17212.

(26) Beidaghi, M.; Wang, C. L. *Adv. Funct. Mater.* **2012**, *22*, 4501−4510.

(27) Luo, J. Y.; Jang, H. D.; Huang, J. X. *ACS Nano* **2013**, *7*, 1464−1471.

(28) Liu, F.; Song, S. Y.; Xue, D. F.; Zhang, H. J. *Adv. Mater.* **2012**, *24*, 1089−1094.

(29) Xu, Y. X.; Sheng, K. X.; Li, C.; Shi, G. Q. *ACS Nano* **2010**, *4*, 4324−4330.

(30) Xu, Z. W.; Li, Z.; Holt, C. M. B.; Tan, X. H.; Wang, H. L.; Amirkhiz, B. S.; Stephenson, T.; Mitlin, D. *J. Phys. Chem. Lett.* **2012**, *3*, 2928−2933.

(31) Zhang, X. T.; Sui, Z. Y.; Xu, B.; Yue, S. F.; Luo, Y. J.; Zhan, W. C.; Liu, B. *J. Mater. Chem.* **2011**, *21*, 6494−6497.

(32) Chen, W. F.; Yan, L. F. *Nanoscale* **2011**, *3*, 3132−3137.

(33) Chen, Y.; Zhang, X.; Yu, P.; Ma, Y. W. *J. Power Sources* **2010**, *195*, 3031−3035.

(34) Cai, M. Z.; Outlaw, R. A.; Butler, S. M.; Miller, J. R. *Carbon* **2012**, *50*, 5481−5488.

(35) Zhang, S. L.; Li, Y. M.; Pan, N. *J. Power Sources* **2012**, *206*, 476−482.

(36) Chen, J.; Sheng, K. X.; Luo, P. H.; Li, C.; Shi, G. Q. *Adv. Mater.* **2012**, *24*, 4569−4573.

(37) Ye, S. B.; Feng, J. C.; Wu, P. Y. *J. Mater. Chem. A* **2013**, *1*, 3495−3502.

(38) Lin, Y. R.; Ehlert, G. J.; Bukowsky, C.; Sodano, H. A. *ACS Appl. Mater. Interfaces* **2011**, *3*, 2200−2203.

(39) Wu, X. Z.; Zhou, J.; Xing, W.; Wang, G. Q.; Cui, H. Y.; Zhuo, S. P.; Xue, Q. Z.; Yan, Z. F.; Qiao, S. Z. *J. Mater. Chem.* **2012**, *22*, 23186−23193.

(40) Park, S.; An, J. H.; Piner, R. D.; Jung, I.; Yang, D. X.; Velamakanni, A.; Nguyen, S. T.; Ruoff, R. S. *Chem. Mater.* **2008**, *20*, 6592−6594.

(41) Yan, Z.; Ma, L. L.; Zhu, Y.; Lahiri, I.; Hahm, M. G.; Liu, Z.; Yang, S. B.; Xiang, C. S.; Lu, W.; Peng, Z. W.; Sun, Z. Z.; Kittrell, C.; Lou, J.; Choi, W. B.; Ajayan, P. M.; Tour, J. M. *ACS Nano* **2013**, *7*, 58−64.

(42) Compton, O. C.; An, Z.; Putz, K. W.; Hong, B. J.; Hauser, B. G.; Brinson, L. C.; Nguyen, S. T. *Carbon* **2012**, *50*, 3399−3406.

(43) Yang, S. J.; Kim, T.; Jung, H.; Park, C. R. *Carbon* **2013**, *53*, 73−80.

(44) Chen, W. F.; Li, S. R.; Chen, C. H.; Yan, L. F. *Adv. Mater.* **2011**, *23*, 5679−5683.

(45) Punckt, C.; Muckel, F.; Wolff, S.; Aksay, I. A.; Chavarin, C. A.; Bacher, G.; Mertin, W. *Appl. Phys. Lett.* **2013**, *102*, 023114.

(46) Tang, L. A. L.; Lee, W. C.; Shi, H.; Wong, E. Y. L.; Sadovoy, A.; Gorelik, S.; Hobley, J.; Lim, C. T.; Loh, K. P. *Small* **2012**, *8*, 423−431.

(47) Fan, Z. J.; Yan, J.; Zhi, L. J.; Zhang, Q.; Wei, T.; Feng, J.; Zhang, M. L.; Qian, W. Z.; Wei, F. *Adv. Mater.* **2010**, *22*, 3723−3728.

(48) Chen, C. M.; Zhang, Q.; Yang, M. G.; Huang, C. H.; Yang, Y. G.; Wang, M. Z. *Carbon* **2012**, *50*, 3572−3584.

(49) Wang, H. W.; Wang, Y. L.; Hu, Z. A.; Wang, X. F. *ACS Appl. Mater. Interfaces* **2012**, *4*, 6826−6833.

(50) Niu, C. M.; Sichel, E. K.; Hoch, R.; Moy, D.; Tennent, H. *Appl. Phys. Lett.* **1997**, *70*, 1480−1482.

(51) Liu, W. W.; Yan, X. B.; Lang, J. W.; Peng, C.; Xue, Q. J. *J. Mater. Chem.* **2012**, *22*, 17245−17253.

(52) Sui, Z. Y.; Meng, Q. H.; Zhang, X. T.; Ma, R.; Cao, B. *J. Mater. Chem.* **2012**, *22*, 8767−8771.

(53) Lin, J.; Zhang, C. G.; Yan, Z.; Zhu, Y.; Peng, Z. W.; Hauge, R. H.; Natelson, D.; Tour, J. M. *Nano Lett.* **2013**, *13*, 72−78.

(54) Kim, J.; Cote, L. J.; Kim, F.; Yuan, W.; Shull, K. R.; Huang, J. X. *J. Am. Chem. Soc.* **2010**, *132*, 818−8186.

(55) Li, Y. Q.; Yang, T. Y.; Yu, T.; Zheng, L. X.; Liao, K. *J. Mater. Chem.* **2011**, *21*, 10844−10851.

(56) Wang, Y.; Shi, Z. Q.; Huang, Y.; Ma, Y. F.; Wang, C. Y.; Chen, M. M.; Chen, Y. S. *J. Phys. Chem. C* **2009**, *113*, 13103−13107.